

# Structural Integrity Analysis of SFR Fuel Cladding During Design Basis Events

Seongchul Park<sup>a</sup>, Seo Yoon Choi<sup>a</sup>, Han Seop Song<sup>a</sup>, Hyung-Kyu Kim<sup>b</sup>, Min-Seop Song<sup>c</sup>,  
Jae-Ho Jeong<sup>a,1</sup>

<sup>a</sup>*Department of Mechanical Engineering, Gachon University, Seongnam, Republic of Korea*

<sup>b</sup>*Korea Atomic Energy Research Institute, Daejeon, Republic of Korea*

<sup>c</sup>*Department of Nuclear Engineering, Hanyang University, Seoul, Republic of Korea*

**Abstract.** A high-fidelity numerical analysis methodology was proposed for evaluating the fuel rod cladding integrity of a Prototype Gen IV Sodium Fast Reactor (PGSFR) during normal operation and Design basis events (DBEs). The MARS-LMR code, system transient safety analysis code, was applied to analyze the DBEs. The results of the MARS-LMR code were used as boundary condition for a 3D computational fluid dynamics (CFD) analysis. The peak temperatures considering HCFs satisfied the cladding temperature limit. The temperature and pressure distributions were calculated by ANSYS CFX code, and applied to structural analysis. Structural analysis was performed using ANSYS Mechanical code. The seismic reactivity insertion SSE accident among DBEs had the highest peak cladding temperature and the maximum stress, as the value of 87 MPa. The fuel cladding had over 40% safety margin, and the strain was below the strain limit. Deformation behavior was elucidated for providing relative coordinate data on each active fuel rod center. Bending deformation resulted in a flower shape, and bowing bundle did not interact with the duct of fuel assemblies. Fuel rod maximum expansion was generated with highest stress. Therefore, it was concluded that the fuel rod cladding of the PGSFR has sufficient structural safety margin during DBEs.

**Keywords.** Structural integrity, PGSFR, fuel assembly cladding, system transient analysis, computational fluid dynamics.

## 1. Introduction

Sodium-cooled fast reactors (SFRs) design technologies were developed in Korea since 1997 to reduce a high-level waste volume and increase uranium resource utilization [1]. In 2015, the preliminary specific design of the Prototype Gen-IV Sodium-cooled Fast Reactor (PGSFR) design was developed, which is a pool-type SFR with thermal power of 392.2 MWt [2, 3]. The basic design concepts of all the structures, systems, and components were determined and incorporated into the preliminary safety information document [4, 5]. It includes the basic design requirements and system descriptions and the results of the safety analysis for representative accident scenarios [5]. The system operates at atmospheric pressure, thus there is no possibility of high-pressure release resulting from pipe breaks, unlike in loop-type LWRs. The large sodium inventory inside

---

<sup>1</sup> Corresponding Author, Jae-Ho Jeong, Department of Mechanical Engineering, Gachon University, Seongnam, Republic of Korea; E-mail: jeaho.jeong@gachon.ac.kr.

the reactor vessel provides a large thermal inertia which relieves the thermal transient and allows a relatively longer grace period under accident conditions. The core outlet temperature is designed to exceed 545 °C as the PGSFR secures 40% thermal efficiency [6, 7]. The PGSFR satisfies the safety acceptance criteria with a sufficient thermal margin during the basis events and is design to prevent from propagating to severe accidents. [1]

The safety objective of PGSFR is to protect the public and the environment from the effects of nuclear radiation. To achieve this goal, PGSFR adopts a defense-in-depth (DID) approach. DID provides inherent safety for all possible accidents, minimizes the possibility of severe accidents, and eliminates the need for extensive evacuation plans by demonstrating low risk to the public and safety. Based on the DID approach, the physical barriers that confine nuclear fission products include fuel cladding, primary coolant boundary, and containment structure. Fuel cladding is the first structure that protects the escape of radiological material to the environment. If the fuel cladding failure occurs, the occurrence possibility of a severe accident exceeding the design basis accident increases. To eliminate the possibility of a severe accident occurring, the structural integrity of fuel cladding must be demonstrated even during the design basis accident.

In nuclear fuel cladding, the high temperature is one factor that reduces structural safety margins of the cladding. During DBEs, the PGSFR fuel assembly operates at high temperatures, approximately 400-800 °C, which are capable of inducing high thermal stresses [8,9]. Thermal expansion with a significant temperature gradient causes the thermal stress of the structure. It is important to determine the blockage area and reduce the possibility of breakage of the cladding [10,11]. When blockage occurs the mass flow rate decreases, leading to increase in the temperature of the coolant and cladding [11]. Disastrous accidents can occur in the nuclear power plant when the cladding is damaged due to leakage of the fissile material and actinide [12]. Therefore, it is important to ascertain the stresses and deformation behaviors of pins to predict further temperature increases and cladding breakage.

Many studies have been conducted to evaluate the structural integrity of PGSFR components. D. L. Porter et al. studied HT-9 cladding creep and stress rupture during the SFR reactor transients [13]. Kim et al. performed an accident analysis of the fuel assembly components of a PGSFR [14]. Yoon et al. analyzed the performance of the nozzles as a function of the internal pressure, thermal load, and external load [15]. Kim et al. performed thermal stress analysis for the plate-type fuel assembly [16]. Kim et al. analyzed the stress experienced by pressure vessels in nuclear power plants [17].

In this paper, a methodology for evaluating the structural integrity of 217-pin cladding in the PGSFR is proposed. Based on the proposed methodology, a three-dimensional simulation is performed to assess the structural integrity of the fuel rod cladding. The MARS-LMR code is applied to analyze DBEs. The results of the MARS-LMR code were used as input boundary condition for a three-dimensional high-fidelity computational fluid dynamics (CFD) analysis. Then, the CFD results such as temperature and pressure distribution on the fuel rod surfaces were applied to structural analysis. Structural analysis was performed using ANSYS Mechanical code based on the finite element method (FEM).

## **2. Description of PGSFR**

The fuel assembly of the PGSFR consists of 217 wire-wrapped fuel rods and a hexagonal duct. The fuel rods are arranged in a hexagonal lattice pattern and are wire-wrapped with

a helical wire spacer to maintain a uniform gap between the rods. The fuel rods are made of uranium-plutonium-zirconium (U-Pu-Zr) metal and are clad in HT-9 stainless steel. The fuel rod diameter is 8.6 mm, the length is 750 mm, and the wall thickness of the cladding is 0.4 mm. The wire spacer is made of HT-9 stainless steel, and diameter is 0.95 mm [12]. The wire spacer is helically wrapped per each fuel rod with regular pattern to assure the gap between rods and prevent the collision [18]. The duct is also made of HT-9 stainless steel and has a hexagonal shape with an inner diameter of 129 mm and a thickness of 5.5 mm. 217 pins of fuel rods are tightly packed in triangular array inside hexagonal duct. The key design parameters of the 217-pin fuel bundle and hexagonal duct are provided in Table 1 and a cross-sectional view thereof is shown in Figure 1 [1]. The wire is wound clockwise from the inlet with a pitch of 199.6 mm, as shown in Figure 1. A cross-sectional drawing of the duct is shown in Figure 2.

**Table 1.** Geometric parameters of The 217-pin fuel assembly

Geometric parameters	Values
Number of fuel pins	217
Pin diameter	7.4 mm
Clad thickness	0.5 mm
Pin pitch	8.436 mm
CFD computation length	1100 mm
Active length of heat region	980 mm
Wire spacer diameter	0.95 mm
Wire lead pitch	221 mm
Coolant	Sodium
Tube flat-to-flat length	126.36 mm
Duct width (outer wall to wall)	132.36 mm
Duc thickness	3 mm
Duct height	1100 mm

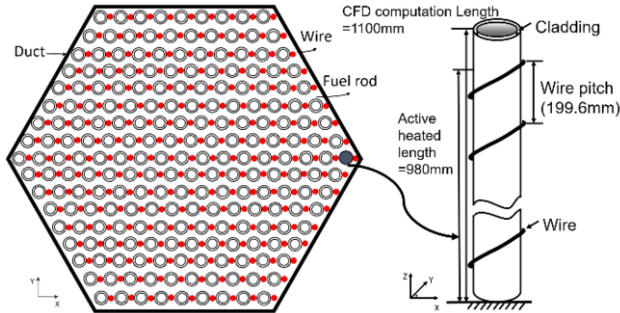


**Figure 1.** Cross-section geometry of the fuel assembly and single fuel pin with the wire.

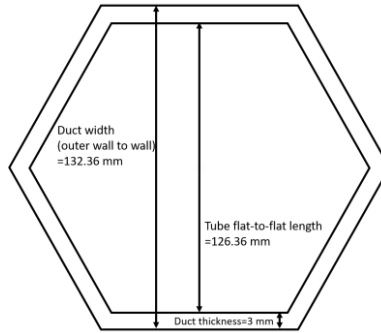


Figure 2. Cross-section geometry of the hexagonal duct.

### 3. Accident Scenarios

Postulated events that may occur during power plant operation are selected in the design stage. The consequences of these events on the plant system and surrounding environment are quantitatively analyzed and evaluated. The PGSFR safety acceptance criteria of the fuel and cladding are summarized in Table 2 [1]. DBEs are classified according to their frequency of occurrence. The safety of the plant design is eventually demonstrated with a margin sufficient to ensure public safety and health based on the safety acceptance criteria described in Table 2.

During normal operation and anticipated operational occurrence (AOO), it is important to prioritize demonstrating structural integrity. AOO events occur once or rarely over the lifespan of a nuclear power plant. They cause minimal damage to the plant's lifespan and nuclear fuel characteristics, and the plant returns promptly to normal operating conditions. As AOO accidents have the highest frequency of occurrence among the DBEs, a representative accident, such as the Spurious PHTS pump trip event, is chosen to demonstrate the structural safety margin of the fuel cladding. The structural integrity of the fuel cladding is evaluated for DBA Class II accidents, which are less frequent but pose a greater threat to the power plant. Evaluating the structural integrity of the cladding for the DBA Class II accidents, such as the Single PHTS pump seizure and Seismic reactivity insertion SSE, can demonstrate the structural safety margins for DBA Class I [19,20].

Table 2. Frequency of occurrence and SFR criteria

Frequency/yr	Plant Condition		Fuel, Cladding, Structure, Damage Limit
$F \geq 1 \times 10^{-2}$	AOO	Operation States	- No fuel melting - $CDF_{\Sigma AOO} < 0.05$
$1 \times 10^{-2} > F \geq 1 \times 10^{-4}$	DBA Class I	Accidents conditions	- No fuel melting - $CDF_{each} < 0.05$
$1 \times 10^{-4} > F \geq 1 \times 10^{-6}$	DBA Class II		- Pin coolable geometry - Fuel T < 1237°C - Clad T < 1075°C
$1 \times 10^{-6} > F \geq 1 \times 10^{-8}$	DEC		- Core coolable geometry - No Bulk Sodium Boiling

### 3.1. Spurious PHTS Pump Trip

The Spurious Primary Heat Transfer System (PHTS) pump trip event is evaluated as one of the Design Basis Events (DBEs) to assess the inherent safety of the PGSFR. [19] It is an AOO event in which the coolant pump stops, causing a coast down to slow down due to mechanical failure or power loss of the two PHTS pumps. In this event, the PHTS pump responsible for transferring heat from the reactor core to the steam generator experiences a sudden and unexpected trip, leading to a rapid decrease in the coolant flow rate, which results in a loss of offsite power (LOOP). The scenarios of this accident are summarized in Table 3, and the core condition is the Beginning of Cycle (BOC). At 0.0 seconds, a LOOP occurs, which causes both PHTS pumps to stop, and the coolant flow of the core decreases with the coast-down operation of the pumps. Due to both the decrease in the flow rate and heat transfer to the IHTS, the temperature of the cladding mid-wall rapidly increases. The reactor is tripped by the 'high power to PHTS flow ratio trip' signal. It induces the temperature decreases. Insertion of the control rod assembly starts after 1.35 seconds, and the DHRS dampers are fully opened, with the blower starting to operate. The accident ends when the DHRS heat removal rate is lowered after a collapse heat incident and cools the reactor. As a result, the fuel assembly temperature begins to increase rapidly, and the mid-wall temperature of the fuel cladding can exceed the safety limit, potentially causing cladding damage and breakage.

**Table 3.** Sequential progression of spurious PHTS pump trip event

LOF Accident	Time(sec)
Inertial operation of two pumps of the primary heat transfer system	0.0
Reach the reactor stop setpoint (high power to PHTS flow ratio trip)	1.18 (110 %)
Start inserting control rod assembly	2.53
Residual heat removal system starts	3.85

### 3.2. Single PHTS pump seizure

An accident involving the seizure of single PHTS pump is a Class II Design Basis Event (DBE) that occurs due to the failure of a mechanical bearing or an electric motor, resulting in the seizure of one PHTS pump. [20] Table 4 summarizes the events that follow this accident. The core condition at the time of the accident is the Beginning of Cycle (BOC). The temperature of the cladding mid-wall increases during the accident due to reduced core coolant flow caused by the seized PHTS pump and the coast down of the other PHTS pump at 0 second. Isolation of the pump and feed water valve of the Intermediate Heat Transfer System (IHTS) causes loss of the heat removal system of the steam generator. The reactor is tripped by the 'high power to PHTS flow ratio trip' signal at 0.03 seconds, and insertion of the control rod assembly begins at 1.33 seconds. Heat removal is carried out solely by the residual heat removal system, which begins operating at 40.29 seconds. At 4,805 seconds, the heat removed by the residual heat removal

system exceeds the heat generated from core decay, resulting in a continuous decrease in the core outlet temperature.

**Table 4.** Sequential progression of Single PHTS pump seizure.

<b>LOF Accident</b>	<b>Time(sec)</b>
Accident occurrence	0.0
Reach the reactor stop setpoint (high power to PHTS flow ratio trip)	0.03 (110 %)
Start inserting control rod assembly	1.33
Residual heat removal system starts	40.29

### 3.3. Seismic Reactivity Insertion SSE(Safe shutdown earthquake)

The event is initiated by the insertion of positive reactivity as a result of the core structure compaction due to an earthquake, leading to increases in the core power and the core outlet temperature. [19] The SSE is a more severe condition than the OBE (Operating Basis Earthquake). The events following the incident are summarized in Table 5, with the core being in the BOC condition. Reactivity insertion of 0.579 \$ for 0.1 seconds is adopted at BOC condition. At 0.0 seconds, the core power increases due to the positive reactivity insertion caused by the earthquake. The SSE-induced LOOP is assumed to occur at the same time. As the core power increases, the 'high neutron flux change rate trip' signal reaches the trip setpoint at 0.06 seconds, and the insertion of control assemblies starts at 0.66 seconds. At the same time as the reactor trip signal is generated, then the PHTS pumps stop, and the reactor coolant flow decreases with the coastdown operation of the PHTS pumps. Insertion of the control rod assemblies then starts. The heat removal capability of the steam generator is lost due to the stoppage of the feed water pump, but the heat generated by the IHTS pump and the residual heat of the reactor is removed by the residual heat removal system. The system damper opens, and the blower operates, causing the temperature of the reactor to continuously decrease to maintain a safe state.

**Table 5.** Sequential progression of insertion of reactivity due to SSE.

<b>TOP Accident</b>	<b>Time(sec)</b>
Accident occurrence	0
Reach the reactor stop setpoint (Variable over-power)	0.06
Start inserting control rod assembly	0.66
Residual heat removal system starts	28.2

## 4. Methodology and Modeling for High-fidelity 3D Numerical Simulation

### 4.1. Overview of the Proposed Methodology for Evaluating Structural Integrity

Figure 3 illustrates the procedure employed to evaluate the structural integrity of the fuel assembly components. Initially, the 217 wire-wrapped fuel rods and hexagonal ducts were modeled for the 3D high-fidelity numerical analysis. The nosepiece, upper, and lower reflectors were excluded from the analysis. The MARS-LMR code was applied to analyze the DBEs. The hot channel factors (HCFs) were considered to evaluate the thermal margin. The results of the temperature and pressure distribution in the radial direction of the fuel assembly cladding were confirmed. The CFD was performed to derive the temperature and pressure distributions of the fuel rods during normal operation and DBEs using MARS-LMR code results. The structural analysis was performed when the cladding temperature reaches its peak. The CFD results such as temperature and pressure distributions were applied for the structural analysis. Using ANSYS Mechanical software, the structural analysis was then applied to calculate the stress and strain of the cladding during DBEs. Finally, the stress and strain values were compared to the stress limit and strain criteria to evaluate the structural integrity.

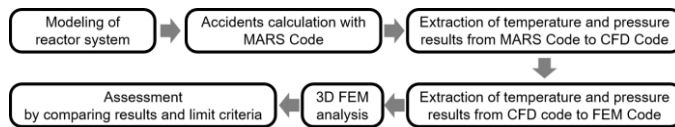


**Figure 3.** Flowchart of system-related finite analysis.

### 4.2. High-fidelity CFD and Structural Analysis Modeling

The RANS based CFD methodology is the grid generation using the Fortran-based in-house code and the GGI function using general-purpose commercial CFD code, CFX. [21] Adopting the innovative grid generation method, there is no displacement between the real wire and rod, thus minimizing grid skewness. Fuel bundle geometries such as the diameter of the rod and wire are fully simulated without any trimmed shape around the contact region between the rod and wire surface. Since the patches nodes on each side of the inner fluid region and the outer fluid region is not matching one to one, the GGI function in CFX code is adopted for this study [22,23]. For this reason, hexahedral meshes with the GGI function can have much longer lengths in the axial direction than those without the GGI function in maintaining the real wire shape and minimizing cell skewness. It can make that the number of hexahedral meshes is fewer than other grid generation methods with hexahedral meshes. Figure 4 shows the mesh of 217 fuel rods. The number of meshes for 3D high-fidelity numerical simulation is 50 million. The minimum grid scale on the fuel rod wall surface was  $5.0 \times 10^{-7}$  m to capture the laminar to turbulent flow transition with the SST turbulence model; the friction velocity  $y^+$  is close to one. The simulation results obtained using this methodology have demonstrated accurately predicting the pressure drop and flow analysis of nuclear fuel assemblies [23].

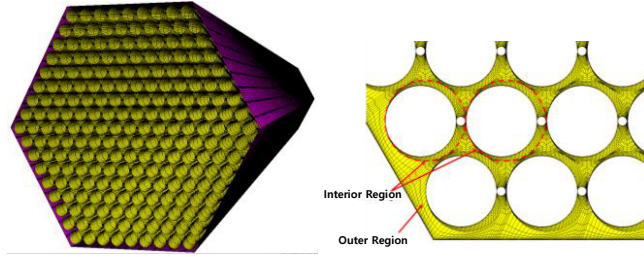


Figure 4. Computational grid system of the fuel assembly (a) perspective view, (b) cross sectional view.

#### 4.3. Boundary Conditions and HT-9 Properties for Structural

The fuel rods are mounted on a vertical mounting rail located inside the hexagonal duct of the lower cap [14]. The bottom part of the model, including the duct, claddings, and wires, is clamped, whereas a gap is provided at the top end of the model to allow for fuel expansion [24]. The nodes at the upper side of the model have three degrees of freedom in translation and three in the rotation that are not constrained. The wire and fuel rod are assumed to be in contact, and the model adopts a normal hard and tangential frictionless contact property for the fuel rod and wire. The applied boundary conditions for the model are presented in Figure 5. The internal pressure of the fuel rod is 6.39MPa to conservatively evaluate the structural integrity of the cladding. It is the highest pressure for End Of Cycle(EOC) with a significant amount of fission products.

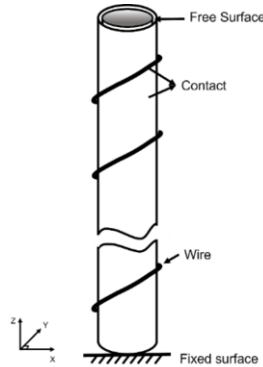


Figure 5. Boundary conditions for structural analysis.

The properties of the material required for the static-thermal structural analysis are Young’s modulus, Poisson’s ratio, density, coefficient of thermal expansion, and thermal conductivity. The properties of HT-9 are calculated using the eqs. 14-18. [25]

- Young’s modulus ( $0^{\circ}\text{C} < T < 800^{\circ}\text{C}$ )

$$Y = 2.137 \times 10^5 - 102.74 \times T \tag{1}$$

- Poisson’s ratio

$$\nu = 0.221956 + 2.643235 \times 10^{-4} \times T - 2.028888 \times 10^{-7} \times T^2 \tag{2}$$

- Density ( $0^{\circ}\text{C} < T < 800^{\circ}\text{C}$ )

$$\rho = 7.778 \times 10^{-3} - 3.07 \times 10^{-1} \times T \tag{3}$$

- Coefficient of thermal expansion ( $0^\circ\text{C} < T < 800^\circ\text{C}$ )

$$C_p = [-1.6256 \times 10^{-3} + 1.62307 \times 10^{-6} \times T + 1.42357 \times 10^{-8} \times T^2 - 5.50344 \times 10^{-12} \times T^3] / T \tag{4}$$

- Thermal Conductivity

$$k = 29.65 - 6.668 \times 10^{-2} \times T + 2.184 \times 10^{-4} \times T^2 - 2.527 \times 10^{-7} \times T^3 + 9.621 \times 10^{-11} \times T^4 \tag{5}$$

## 5. Results and Discussion

### 5.1. Peak Temperature Result of MARS-LMR Code

The temperature of the cladding mid-wall, power, and mass flow during normal operation and DBES was calculated using the MARS LMR code. The temperature of the coolant, cladding, and fuel for the hottest nuclear fuel rod is conservatively calculated by considering hot channel factors.

In steady normal operation, the mid-cladding temperature is  $574^\circ\text{C}$ . Considering the HCFs, it is  $605.7^\circ\text{C}$ . To evaluate conservatively, the thermal margin is over  $450^\circ\text{C}$ , the difference between the peak temperature considering HCFs and the criteria applied for DBA Class II. The cladding temperature is shown in figure 6.

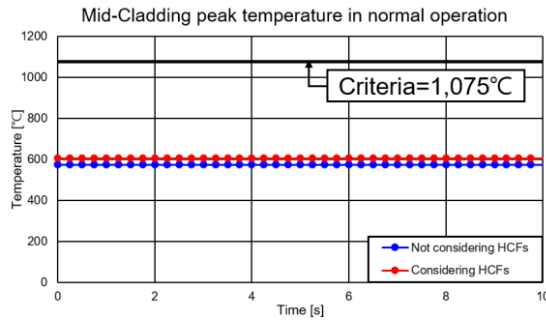


Figure 6. Mid-Cladding peak temperature in normal operation.

The MARS-LMR code was used to simulate the 'Spurious PHTS pump trip' with initial conditions that produce the most conservative results. The event can be initiated by a spurious PHTS pump trip due to LOOP, leading to a rapid reduction in coolant flow rates. Flow rates reduction induces the cladding temperature increase, shown as Figure 7. In figure 7, the temperature of the cladding mid-wall increases and reaches the peak temperature, after which it gradually decreases with the insertion of the control rod assemblies at 2.6 seconds. At 2.6 seconds, the temperature of the cladding mid-wall reaches a peak of  $599.9^\circ\text{C}$ . If the peak temperature is calculated while considering HCFs, it increases to  $636.3^\circ\text{C}$ . This margin exceeds the allowable standard temperature of  $1,075^\circ\text{C}$  by more than  $400^\circ\text{C}$ . At the peak temperature of the cladding mid-wall, the flow rate is  $18.18\text{ kg/s}$ , and the total power is  $4330.38\text{ kW}$ .

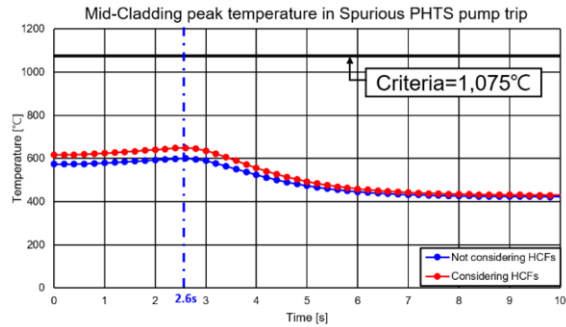


Figure 7. Mid-Cladding peak temperature in Spurious PHTS pump trip.

The MARS-LMR code was used to simulate 'Single PHTS pump seizure' with initial conditions that yield the most conservative results. The event is initiated by a dramatic decrease in core coolant flow rates due to a single PHTS pump seizure, leading to increases in core power and the core outlet temperature. Figure 8 shows the temperature of the cladding mid-wall, including the temperature when considering HCFs. The temperature of the cladding mid-wall increases and reaches its peak value, after which it decreases with the insertion of the control rod assemblies. At 1.75 seconds, the peak temperature of the cladding mid-wall is 655.32 °C. Considering HCFs, the peak temperature rises to 715.45 °C. It has 33 % margin from the cladding temperature criteria of DBA Class II, 1,075°C. At the peak temperature of the cladding mid-wall, the flow rate is 12.07 kg/s, and the total power is 2861.2 kW.

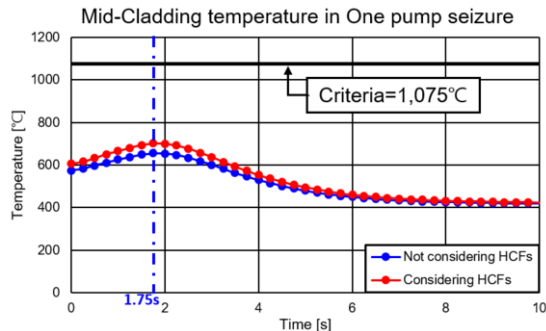


Figure 8. Mid-Cladding peak temperature in Single PHTS pump seizure.

Seismic Reactivity Insertion-SSE was simulated using the MARS-LMR code with the initial conditions that derive the most conservative results. The event is initiated by the insertion of positive reactivity as a result of the core structure compaction due to an earthquake, leading to increases in the core power and the core outlet temperature. Figure 9 shows the temperature of the cladding mid-wall with and without consideration of the HCFs. At the same time as the reactor trip signal is generated, then the PHTS pumps stop, and the reactor coolant flow decreases with the coastdown operation of the PHTS pumps. As the flow rate decreases, the temperature of the mid-wall of the cladding increases. It decreases after the control fuel assemblies insert. The peak temperature of the cladding mid-wall reaches 673.69 °C at 1.06 sec, and 717.94 °C, considering the HCFs. It has a

margin of more than 350 °C from the criteria of cladding temperature for DBA Class II, 1,075 °C. When the temperature of the cladding mid-wall reaches the peak, the flow rate and power are 21.31 kg/s and 5116.72 kW, respectively.

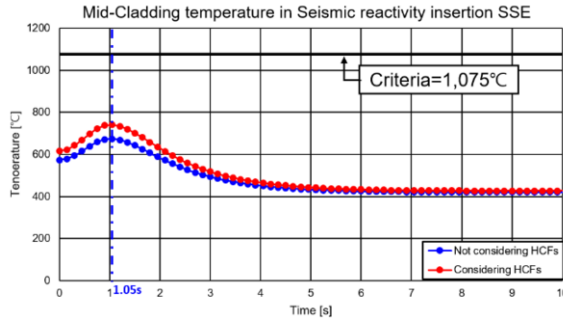
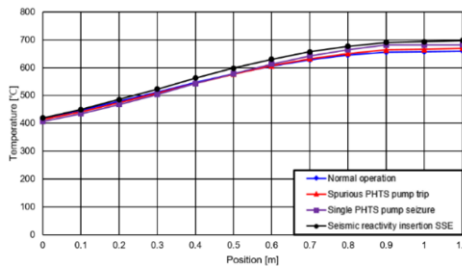


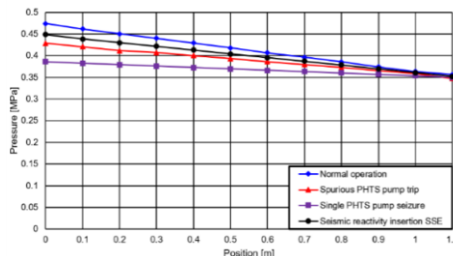
Figure 9. Mid-Cladding peak temperature in Seismic reactivity insertion SSE.

5.2. Temperature and Pressure Distribution Results of ANSYS CFX Code

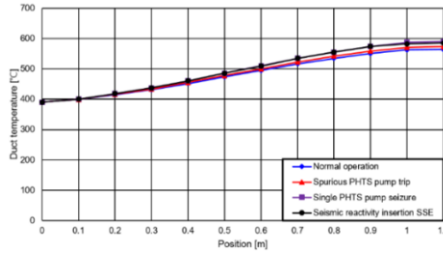
The simulation results of the MARS-LMR code were used as boundary conditions for high-fidelity CFD analysis. The CFD results required for structural analysis are the temperature and pressure distribution of fuel rods. Figure 10-a shows the temperature of the fuel rods at each positions in the vertical direction, and the pressure is plotted in Figure 10-b. The temperature of the duct at various elevations from the base of the fuel rod is given in Figure 10-c. As the elevation increases from the bottom, the temperature increases while the pressure decreases. The temperature and pressure distribution of the highest temperature case is shown in figure 11 that the results are applied to the model. The case is seismic reactivity insertion-SSE.



(a)



(b)



(c)

Figure 10. CFD results of 217 pin fuel rods at each elevations during normal operation and DBEs (a) temperature distribution in fuel rods, (b) pressure distribution in fuel rods, (c) temperature distribution of duct.

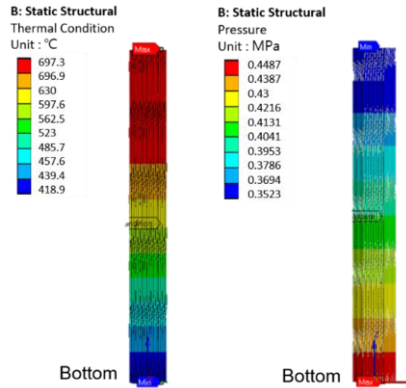


Figure 11. Temperature and Pressure distribution of 217 pins during Seismic reactivity insertion SSE.

### 5.3. Results of Structural Analysis

The structural integrity of the fuel rod cladding was evaluated by comparing the maximum stress during normal operation and DBEs with the stress limits. The stress limits of the PGSFR fuel assembly components were developed considering the previous studies [26]. The stress limit is calculated by using yield strength and ultimate strength. The stress limit varies with temperature, as shown in Figure 12. The Level A corresponds to normal operation and refueling, while Level B corresponds to DBA Class I, Level C to DBA Class II, and Level D to DEC (Design Extended Condition) [8]. As shown in Figure 13, the highest stress is located at the top, which is considered to be the location with the highest temperature. It can be confirmed that the maximum stress occurs in the area close to the wire among the fuel rods. The pattern of maximum stress occurrence was observed in all analyzed accidents as well as during normal operation. The stress results for the case of seismic reactivity insertion SSE, which has the highest stress, are summarized in figures 14 and 15. Figure 14 shows the stress results for the entire model, indicating that the highest stress is located at the top. Figure 15 shows the sectional stress results of cross section at 0.3 m, 0.6 m, 0.9 m, and 1.1 m. In figure 15, as the height increases the stress of cladding also gradually increases.

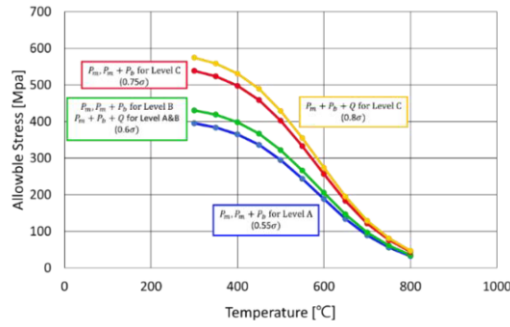


Figure 12. A master curve for design.

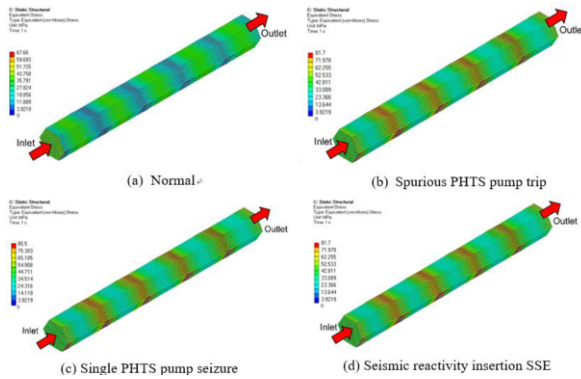


Figure 13 Typical view of the stress concentration in the fuel assembly during normal operation and DBEs.

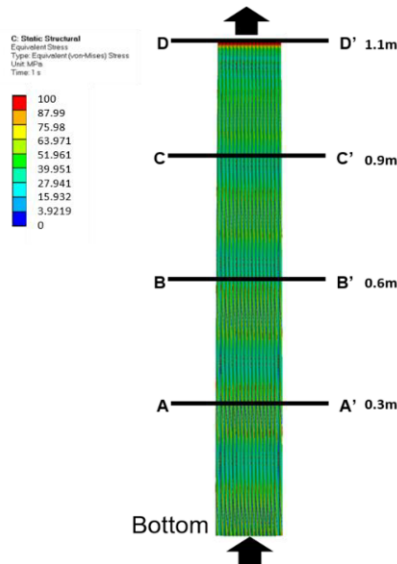


Figure 14 Overview the stress result of 217pins in the case of seismic reactivity insertion SSE.

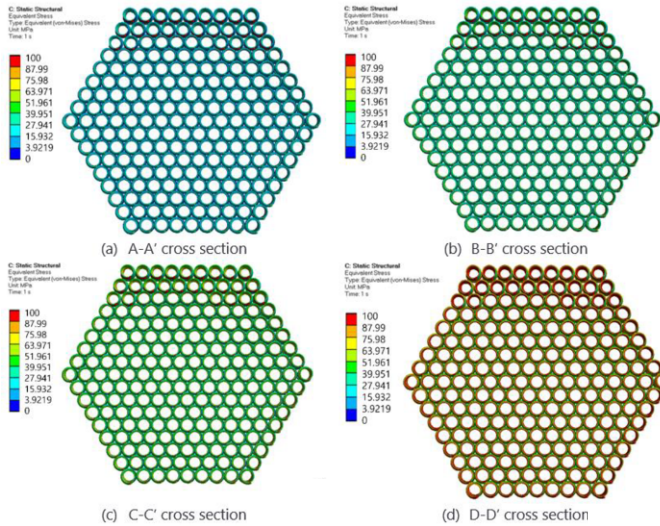


Figure 15 The stress results of the cross section in the case of seismic reactivity insertion-SSE.

The stress distribution according to the height can be checked in Figure 16. This is the linearized stress at the bar where the maximum stress occurs. The graph curve takes the shape of a transverse wave. The crest is the location where the wire passes and the trough is the result of the stress located in the middle between the wires. As the height increases, the temperature increase induce the stress increases.

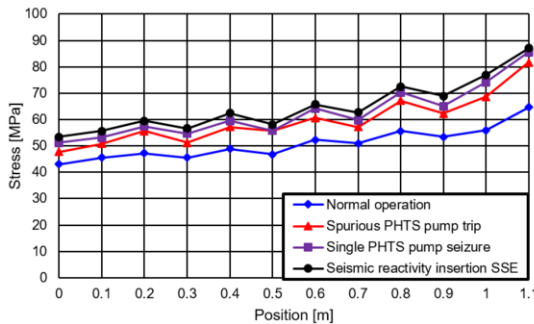


Figure 16 Max stress distribution during normal operation and DBEs.

Table 6 summarizes the maximum stress of the membrane and the sum of membrane and bending stress, in addition to the total stress, stress limit, and safety margins during DBEs. The stress results listed in Table 6 were evaluated by a three-dimensional structural analysis during representative accidents. During normal operation, the maximum total stress, which is sum of the membrane, bending and the thermal stress, is 64.66 MPa. The maximum total stress during a spurious PHTS pump trip event is 81.7 MPa, with a safety margin of 52.8% from the stress limit. During Single PHTS pump seizure and SSE reactivity insertion events, the maximum total stresses are 85.5 MPa and 87 MPa and the safety margins are 62.9% and 47.6% from the stress limit, respectively. The maximum membrane stresses are lower than the yield strength, inducing linear

elastic deformation. The total stress generated is the highest in the seismic reactivity insertion SSE accident during operation at the highest temperature. The maximum stress of the cladding satisfies the stress limit, securing enough safety margin of 47%. The result of evaluating the stress in two representative cases corresponding to DBA Class II led to the conclusion that all of the parameters enable safe operation.

**Table 6.** Stress analysis and comparison with stress limits for normal operation and DBEs.

Condition		Pm	Pm+Pb	Pm+Pb+Q
Normal	Min stress limit [MPa]	222 (<0.55 $\sigma_u$ at 569 °C)		242.3 (<0.6 $\sigma_u$ at 569 °C)
	Max Stress [MPa]	36.62		67.66
	Safety Margin [%]	83.5		72

Strain is one of the primary parameters that determine the fuel design limit. In SFRs, the allowable nuclear fuel design limit is applied at a strain rate of 1% for DBEs. [1] Figure 17 shows the strain results according to height. In all accidents, the maximum strain is lower than the 1% strain limit. Therefore, the cracking of the oxide film is not induced, which is significant because radial cracking of the oxide film can cause stress concentration at the crack tip, leading to the initiation of cracks in the cladding. [27] Since the strain is much lower than the limit, the risk of cladding failure is considered to be low.

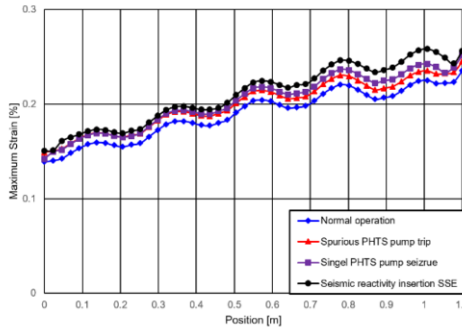


**Figure 17** Maximum strain distribution during normal operation and DBEs.

According to the strain results, the maximum strain was found to be at the top where the stress was the highest. To investigate the deformation behavior at the end, the cross section of the fuel rods at 1.1m was shown in figure 17 during seismic reactivity insertion SSE. In figure 18, the bowed bundle partly interacts with the wire spacer of adjacent bowed bundle. It was observed that bending deformation increased outward from the center of the bundle, resulting in a flower shape. This is because the rods in the center act as barriers to each other, causing less bending deformation. The farther the pin is away from the center of bundle, the greater the degree of local transverse bending deformation. As the distance between rods increases, some neutrons may be absorbed or escape as they have to pass through more mass. Therefore, the neutron effectiveness decreases as the distance increases [28]. The bending deformation of the fuel pins induces a change in the fuel area. If the fuel area decreases, the flow rate and heat

capability decrease. [29] Reducing flow area decreases the flow rate of the fluid for heat exchange. Impeded fluid cooling results additionally in local overheating, which could give rise to fin deformation and narrowing of the flow channels. [30] However, the bowed bundle partly interacts with the wire spacer of adjacent bowed bundle.

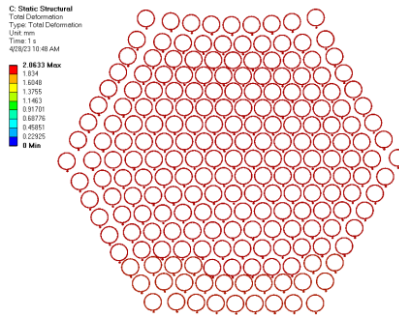


**Figure 18** Bending deformation result at 1.1 m during Seismic reactivity insertion SSE.

To ensure the possibility of contact between the outermost rods and the duct due to the bowing of the rods, the pin-to-duct clearance was calculated. For a specific section of an assembly, the pin-to-duct clearance is defined as the distance from the duct to the nearest point in the cladding section. The definition of the pin-to-duct gap is illustrated in Figure 19 [30].

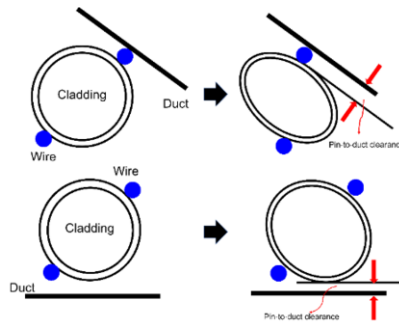


**Figure 19** Diagrammatic definition of the pin-to-duct clearance.

The dependence of the minimum pin-to-duct clearance on the axial position is plotted in Figure 20[30]. The pin-to-duct clearance decreases with increasing temperature, which is accompanied by an increase in the generated stress and strain. Therefore, the pin-to-duct gap at the top of the model with the highest temperature is the lowest. During normal operation and DBEs, the bowing bundle did not interact with the duct of fuel assemblies.

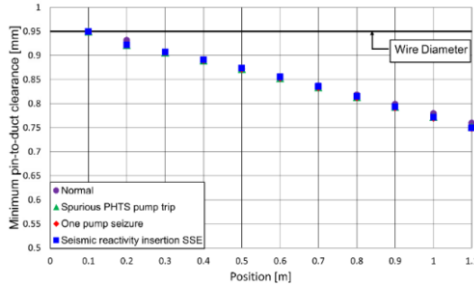


Figure 20 Minimum pin-to-duct clearance along position during normal operation and DBEs.

The calculation of ovality was conducted as a means to analyze expansion, which is one of the factors that can compromise structural integrity. Oval deformation of the cladding is caused by the compression of adjacent wires. Due to the expansion of the spacer wires, the cross-sectional shape of the cladding changes. To quantitatively evaluate the oval deformation of the claddings, the maximum ovality of the top of bundle. The ovality  $\Delta D$  is defined as follows:

$$\Delta D = D_f - D_n \tag{21}$$

where  $D_f$  and  $D_n$  are the distances between the farthest two points and the nearest two points [30]. A more detailed and intuitive definition of  $D_f$  and  $D_n$ , as well as the ovality, is illustrated in Figure 21 [30]. Table 7 summarizes the maximum  $\Delta D$  in the top plane for each operating condition. The highest  $\Delta D$  was confirmed to prevail in the seismic reactivity insertion SSE event operating under the highest temperature condition. This means that the expansion occurs easily.

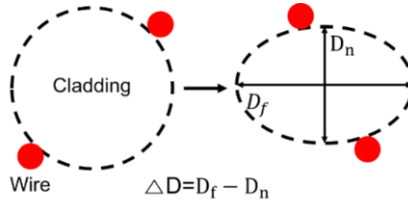


Figure 21. Schematic diagram of oval deformation of the cladding and definition of the ovality.

Table 7. Minimum ovality at the 1.1m during normal operation and DBEs.

	Normal	Spurious PHTS pump trip	Single PHTS pump seizure	Seismic reactivity Insertion SSE
$\Delta D$	0.06	0.12	0.14	0.22

## 6. Conclusion

In this study, the integrity of fuel rod cladding in PGSFR fuel assembly was evaluated by conducting a high-fidelity 3D numerical simulation for normal operation and DBEs such as spurious PHTS pump trip, single PHTS pump seizure, and seismic reactivity insertion SSE. The deformation behavior of the cladding was also elucidated for

providing relative coordinate data on each active fuel rod center to calculate core reactivity insertion

The evaluation results of Structural integrity of cladding are follows:

1. The peak temperature considering HCFs of the PGSFR fuel assembly is lower than 1,025 °C of the cladding temperature limit during all DBEs.
2. The maximum stress of the cladding satisfies the stress limit, thus the cladding secures enough safety margin of 47%.
3. The radial strain of the cladding is much lower than 1% of the strain limit.
4. The bending stress and the bending deformation increases from the center to the outer edge of the fuel rod bundle.
5. The radially bowed bundle located near the duct wall does not interact with the duct of fuel assemblies. However, the bowed bundle interacts with the wire spacer of adjacent bowed bundle.
6. The deformation due to fuel rod expansion has largest value in the highest temperature during seismic reactivity insertion SSE.

Based on these analysis results, it is concluded that the structural integrity of the fuel rod cladding in PGSFR fuel assembly is guaranteed during normal operation and DBEs.

## Acknowledgment

This work was supported by Korea Institute of Energy Technology Evaluation and Planning(KETEP) grant funded by the Korea government(MOTIE)(RS-2023-00243201, Global Talent Development project for Advanced SMR Core Computational Analysis Technology Development)

## References

- [1] K. L. Lee., K.-S. Ha., J.H. Jeong., C.-W. Choi., T. Jeong, S. J. Ahn., S. W. Lee., W.-P. Chang, S. H. Kang, J. Yoo, A Preliminary Safety Analysis for the Prototype Gen IV Sodium-Cooled Fast Reactor, Nuclear Engineering and Technology 48 ,2016, pp. 1071-1082.
- [2] D. Hahn, Y.-I. Kim, C.B. Lee, S.-O. Kim, J.-H. Lee, Y.-B. Lee, B.-H. Kim, H.-Y. Jeong, Conceptual design of the sodium cooled fast reactor KALIMER-600, Nuclear Eng. Technol. 39, 2007, pp. 193-206.
- [3] D. Hahn, J.-W. Chang, Y.I. Kim, Y.-B. Lee, Advanced SFR design concepts and R&D activities, Nuclear Engineering and Technology 41 2009, pp. 427-446.
- [4] System Description of Prototype Gen-IV Sodium-cooled Fast Reactor, SFR-000-SP-403e001, Korea Atomic Energy Research Institute, 2015.
- [5] Preliminary Safety Information Document of PGSFR, Korea Atomic Energy Research Institute, 2015.
- [6] J. Yoo, J. Chang, J.-Y. Lim, J.-S. Cheon, T.-H. Lee, S. K. Kim, K. L. Lee, H.-K. Joo, Overall system description and safety characteristics of prototype Gen IV sodium cooled fast reactor in Korea, Nuclear Eng. Technol. 48, 2016, pp. 1059-1070.
- [7] T. W. Kim, K.-S. Ahn, J.-H. Baek, Y.-G. Kim, W.-S. Park, Overview of PGSFR Project. Am. Nucl. Soc. 114(1), 2016, pp. 698-699.
- [8] Hyung-Kyu Kim, Kyung-Ho yoon, Young-Ho Lee, Hyun-seong lee, jin-sik cheon, Mechanical design of a sodium cooled fast reactor fuel assembly in Korea: Normal operation condition, Nuclear Engineering and Design 346, 2019, pp.67-74.
- [9] Yun Chang Lee, Ju Chan Lee, Seok Jin Oh, Chang Kyu Kin, Analysis of Heat transfer and thermal stress on new shape of hanaro fuel, Transaction of the Korean Nuclear society, 2004.

- [10] Study on the standard establishment for the integrity assessment of nuclear fuel cladding materials, KAERI.
- [11] Thermal-hydraulics analysis of flow blockage events for fuel assembly in a sodium-cooled fast reactor, Peng Du, Jianqiang Shan, Bo Zhang, Laurence K.H. Leung, International Journal of Heat and Mass Transfer 138, 2019, pp. 496-507.
- [12] NSSS Design and validation of prototype GEN-IV Sodium Cooled Fast Reactor, KAERI, 2018.
- [13] D. L. Porter and D. C. Crawford, Fuel Performance Design Basis for the Versatile Test Reactor, American Nuclear Society 196, 2021, pp. 110-122.
- [14] K.H. Yoon, H.-K. Kim, H.S Lee, J.S. Cheon, Component design and accident analysis fuel assembly for prototype GEN-IV sodium-cooled fast reactor, Nuclear Eng. Design 340, 2018, pp. 133-145.
- [15] H.S. Yoon., J. M. Kim., C.S. Maeng., H. M. Kim, Two- and Three-Dimensional Analysis Comparison of Nozzles due to Internal Pressure, Thermal Load and External Load, J. Comput. Struct. Eng. Inst. Korea, 28(3), 2015, pp. 283-291.
- [16] K.S. Kim., J. S. Ryu., J. H. Oh., J. M. Lee., C. Y. Lee., Thermal Stress Analysis for the Plate Type Fuel Assembly, Transactions of the Korean Nuclear Society Spring Meeting 2010.
- [17] Kim Cheong Uk, Ju Yeong Woo, Stress Analysis of Pressure Vessels in Nuclear Power Plants (Part II: Stress Analysis of Tapered Cylinder in the Shell-Head Junction, Journal of Mechanical Science and Technology, 16(2), 1976, pp. 202-209.
- [18] Jeong, Yeong Shin, Bang, In Cheol Park, Seong Dae, Thermal-Hydraulic Effect of Pattern of Wire-wrap Spacer in 19-pin Rod Bundle for SFR Fuel Assembly, Korean Nuclear Society Spring Meeting, 2016.
- [19] Jae-ho jeong, Sung-Jun Ahn, Jonggan Hong, Seok-Hun Kang, Comparative Safety Analysis with MARS-LMR and SAS4A/SASSYS-1 codes for PGSFR, in: Transaction of the Korean nuclear society spring meeting, Jeju, May 23-24, 2019.
- [20] Ji-Youn kim, Jae-Ho Jeong, Chi-Woong Choi, Tae-Kyung Jeong, Sang-Jun Ahn, Kwi-Lim Lee, Safety Analysis of One Pump Seizure Accident for 2017 PGSFR related to Effect of Pump Seizure Time and Loss of Off-site Power, in: Transaction of the Korean Nuclear Society Autumn Meeting, Gyeongju, Oct 26-27, 2017.
- [21] Jae-Ho Jeong, Min-Seop Song, Kwi-Lim Lee, RANS based CFD methodology for a real scale 217-pin wire-wrapped fuel assembly of KAERI PGSFR, Nuclear Engineering and Design 313, 2017, pp. 470-485.
- [22] Min seop song, Jae ho jeong, Eung soo kim, Numerical investigation on vortex behavior in wire-wrapped fuel assembly for a sodium fast reactor, Nuclear Engineering and Technology 51, 2019, pp. 665-675.
- [23] Jae-Ho Jeong, Min-Seop Song, Kwi-Lim Lee, Thermal-hydraulic effect of wire spacer in a wire-wrapped fuel bundles for SFR, Nuclear Engineering and Design 320, 2017, pp. 28-43.
- [24] Donny Hartanto, Chilhyung Kim, Yonghee Kim, A comparative physics study for an innovative sodium-cooled fast reactor (iSFR), International journal of energy research, 2018, pp. 151-162.
- [25] J. D. Hales, R. L. Williamson, S. R. Novascone, G. Pastore, B. W. Spencer, D. S. Stafford, K. A. Gamble, D. M. Perez, R. J. Gardner, W. Liu, J. Galloway, C. Matthews, C. Unal, N. Carlson BISON Theory Manual the Equations Behind Nuclear Fuel Analysis. BISON Release 1.3, 2016.
- [26] Kim, H. K., et al., Fuel Assembly Mechanical Design Report, KAERI (in Korean), SFR-170-FP-475-020, Rev. 0, 2018.
- [27] S.-S. Kang, S.-H. Kim, Y.-K. Jung, C.-Y. Yang, I.-G. Kim, Y.-H. Choi, H.-J. Kim, M.-W. Kim, B.-H. Rho, Study on the Standard Establishment for the Integrity Assessment of Nuclear Fuel Cladding Materials, Technical Report KAERI/CM-1034/2007, 2008.
- [28] Nuclear Reactor Analysis (J. J. Duderstadt, L. J. Hamilton, 2nd Edition).
- [29] X. Ye, F. Gao, X. Chen, X. Liu, Y. G. Wei., Full-scale finite element analysis of deformation and contact of a wire-wrapped fuel bundle subject to realistic thermal and irradiation conditions, Nuclear Eng. Design 364, 2020.
- [30] P. Du, J. Shan, B. Zang, L. K. H. Leung, Thermal-hydraulics analysis of flow blockage events for fuel assembly in a sodium-cooled fast reactor, Int. J. Heat Mass Transfer 138, 2019, pp. 496-507.